Pursuant to the DOE Public Access Plan, this document represents the authors' peer-reviewed, accepted manuscript. The published version of the article is available from the relevant publisher.

ACS APPLIED ENERGY MATERIALS

www.acsaem.org Article

Trap-Assisted Dopant Compensation Prevents Shunting in Poly-Si Passivating Interdigitated Back Contact Silicon Solar Cells

Matthew B. Hartenstein, Caleb Stetson, William Nemeth, Vincenzo LaSalvia, Steven P. Harvey, San Theingi, Matthew Page, Chun-Sheng Jiang, Mowafak M. Al-Jassim, David L. Young, Sumit Agarwal,* and Paul Stradins*

Cite This: https://doi.org/10.1021/acsaem.1c01775 Read Online

ACCESS | Metrics & More | Article Recommendations | Supporting Information

ABSTRACT: Using a trap-assisted compensation model, we explain why polycrystalline Si (poly-Si) passivating contacts are able to achieve low leakage current between the doped fingers of interdigitated back contact (IBC) monocrystalline Si solar cells despite mixing of boron and phosphorus dopants in the isolation region. The fill factor of IBC solar cells is strongly affected by the electrical isolation region between n- and p-type fingers, as this region is critical in minimizing shunting losses. During fabrication of monocrystalline Si solar cells with poly-Si passivating contacts, the intrinsic poly-Si isolation region inevitably gets contaminated with both p- and n-type dopants. Using dopant profiles measured with time-of-flight secondary ion mass spectrometry and scanning probe measurements of the isolation region, we demonstrate that despite the dopant spreading during cell processing, a well-compensated region between the doped fingers exists that prevents shunting. The trap-assisted dopant compensation mechanism significantly widens the compensated region to tens of microns, where the residual dopant densities are below the trap density. This enables a high-resistivity region, resulting in low shunt current. Using one-dimensional (1-D) finite element diode simulations, we identify the design parameters and experimental conditions under which a sufficiently resistive region can form. Our measurements of 2-D local resistivity and work function maps across the isolation region using scanning spreading resistance microscopy and Kelvin probe force microscopy demonstrate the existence of a highly resistive, wide compensated region and confirm our proposed compensation mechanism. For our structures, this region is ~25 μm in width within a ~150 μm wide finger isolation region with nearly 3 orders of magnitude higher resistivity than the regions dominated by a single type of dopant.

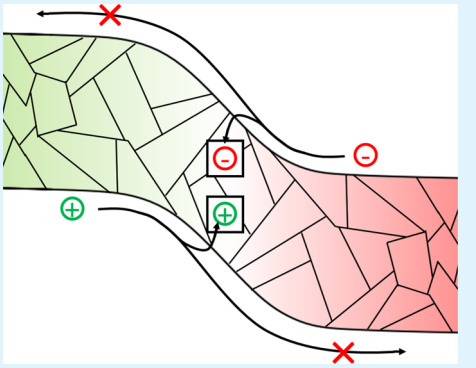

KEYWORDS: *silicon photovoltaics, passivating contacts, interdigitated back contacts, device simulation, dopant compensation*

INTRODUCTION

Solar energy is one of the most promising technologies for meeting the world's ever-growing energy demands, and silicon solar cells currently dominate the photovoltaics (PV) industry at 96% market share.[1] Record high efficiencies in Si PV have been reported using passivating contacts based on polycrystalline silicon on silicon oxide (poly-Si/SiO_x) (26.1%)[2,3] and hydrogenated amorphous silicon (a-Si:H) in silicon heterojunction (SHJ) cells (26.6%),[4,5] applied to high lifetime, n-Cz monocrystalline wafers. Poly-Si/SiO_x contacts chemically passivate the crystalline silicon (c-Si) surface with an ultrathin ~1.4−2.2 nm layer of SiO_x.[6−8] This oxide layer is either thin enough to allow for quantum mechanical tunneling[9−11] and/or has nanoscale pinholes[12] through which charge carriers can transport from the bulk c-Si into the heavily doped poly-Si contacts.[2,9,13−16]

The highest efficiencies for poly-Si/SiO_x and SHJ passivating contact structures are achieved on the interdigitated back contact (IBC) architecture,[4,15,17] wherein both polarities of carrier-collecting contacts are on the rear side of the device. IBC solar cells are a very promising architecture for Si PV due to their high short-circuit current density, J_{sc},[18] which is due to the lack of front shading loss and no parasitic absorption from a-Si:H or poly-Si at the front of the device. IBC cells can also be made bifacial,[19−21] and thus have great potential to enter the mainstream Si PV market. However, more cost-effective, simpler processing techniques are needed, especially for forming highly passivated IBC finger structures at the back of the cell with no shunting. We focus on the poly-Si/SiO_x contacts for IBC cells (see Figure 1a), and in particular the intrinsic poly-Si region separating the n- and p-type fingers (Figure 1b). This region between the two polarities of IBC

Received: June 20, 2021
Accepted: August 24, 2021

Downloaded via NATL RENEWABLE ENERGY LABORATORY on September 13, 2021 at 17:46:01 (UTC).
See https://pubs.acs.org/sharingguidelines for options on how to legitimately share published articles.

© XXXX American Chemical Society

https://doi.org/10.1021/acsaem.1c01775
ACS Appl. Energy Mater. XXXX, XXX, XXX−XXX

Pursuant to the DOE Public Access Plan, this document represents the authors' peer-reviewed, accepted manuscript.
The published version of the article is available from the relevant publisher.

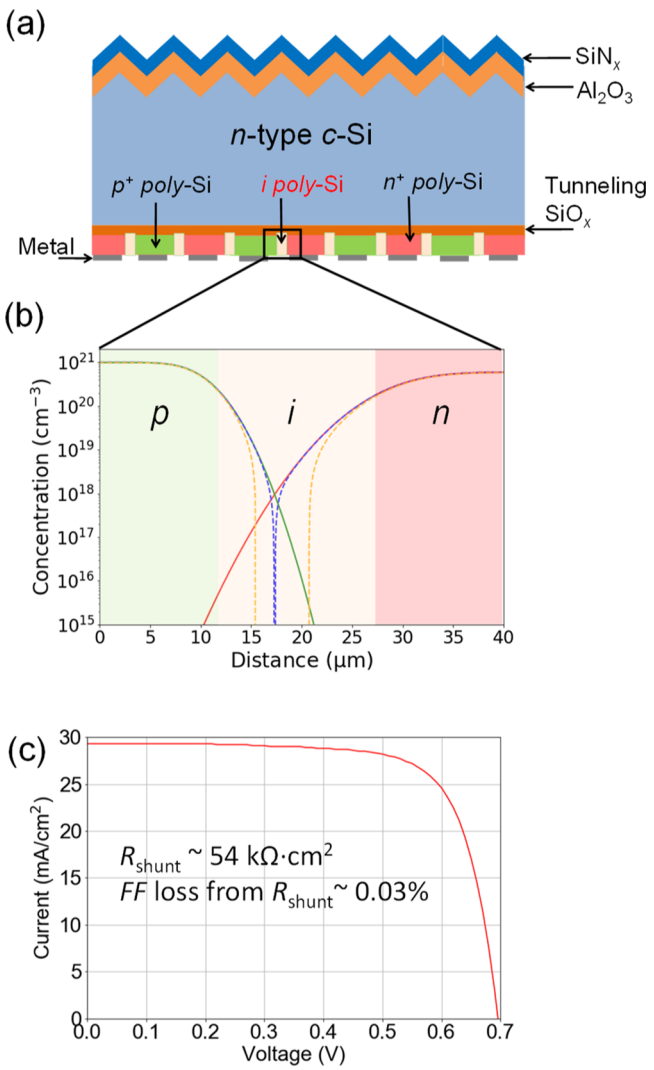

Figure 1. (a) Schematic of the IBC cell structure discussed herein, with poly-Si passivating contacts on the rear of the cell. (b) Concentration profiles of boron (green) and phosphorus (red) extend into the isolation region and overlap. The net carrier concentration for trap densities of $N_t = 10^{17}$ cm^{-3} and $N_t = 10^{19}$ cm^{-3} is shown in blue and orange. (c) A current−voltage curve of an IBC solar cell with a contaminated poly-Si isolation region.

contacts must be well passivated to prevent recombination of charge carriers and well insulating to prevent shunting losses between the doped fingers. In c-Si IBCs based on doped poly-Si contacts, direct contact between p- and n-type regions can lead to significant shunting because of the very high dopant densities (>10^{20} cm^{-3}), and possible tunnel junction formation between the heavily doped regions.[22] According to Green,[23] the cell fill factor FF is reduced due to R_{shunt} according to the equation

$$FF = FF_0\left(1 - \frac{0.84}{R_{shunt}/R_{ch}}\right) \quad (1)$$

where FF_0 is the fill factor if no resistive losses existed, R_{shunt} is the total shunt resistance of the cell, and R_{CH} is the characteristic cell resistance defined as V_{oc}/I_{sc}. To prevent fill factor loss from shunting to below 1% absolute, the shunt resistance of this isolation region must be ~1.5 kΩ·cm^2 or higher for a cell with an open-circuit voltage (V_{oc}) of 700 mV and a J_{sc} of 40 mA/cm^2.[23,24] One method to isolate the n- and p-type doped regions in an IBC device is to create an engineered gap between the two types of doped fingers. However, this requires selective etching of the region between the doped fingers and repassivation of the underlying c-Si wafer in the gap to prevent loss in V_{oc},[22] adding to process complexity and production costs.

While previous studies using simulations have investigated the optimal dimensions, electrical properties, and passivation quality of the doped fingers,[25−29] a majority of these studies regard the region between the intentionally doped fingers as insulating. However, in experimentally fabricated devices, dopants are known to spread into the nominally intrinsic poly-Si isolation region between the n- and p-doped fingers through multiple mechanisms: diffusion during high-temperature annealing steps, incomplete masking, and gas-phase transfer.[24] To mitigate dopant spreading in the isolation region, complicated processing steps would have to be incorporated. In practice, however, record efficiency IBC cells with poly-Si/SiO_x backside contacts and isolation regions have been achieved despite significant contamination of the isolation region with dopants.[15,17] Therefore, an efficient and robust compensation mechanism must exist that prevents shunting the isolation region, which is revealed in this work.

We explore the dopant contamination of the intrinsic poly-Si isolation region from dopant tails originating from the adjacent oppositely dopped fingers (Figure 1b). We consider two types of dopant profiles: error-function-shaped dopant profiles created by lateral diffusion of dopants,[17] or exponential-shaped profiles formed during masked plasma-enhanced chemical vapor deposition (PECVD).[24] While the primary focus of this work is of poly-Si p−i−n structures across doped IBC fingers, this type of structure has been demonstrated for use in other semiconductor devices such as electro-optical devices and coplanar thin film diodes.[30−32] We consider the effect of compensation in this region leading to reduced conductivity due to reduced net free carrier concentration, n_{eff}. Importantly, n_{eff} will be significantly reduced by capture of carriers at grain boundary and bulk defects that are abound in poly-Si.[33−36] We call this trap-assisted compensation. With this mechanism, we determine the necessary conditions for characteristic diffusion length, finger separation, and trap defect density under which an appropriately resistive region will form. Furthermore, we present experimental evidence of this highly resistive region by scanning spreading resistance microscopy (SSRM) and Kelvin probe force microscopy (KPFM). The SSRM reveals that local resistivity increases by several orders of magnitude in a wide (~25 μm) region, where strong, trap-assisted compensation occurs. The KPFM results confirm that a depletion region exists at this dopant compensation point that is of the same wide width as predicted by our simulations and measured by SSRM. As a result, with properly engineered trap-assisted compensation in poly-Si/SiO_x contacts, adding additional processing steps to prevent the dopants from spreading into the isolation region may not be needed during fabrication. This significantly widens the process window and suggests that industrial production of this type of IBC cell would be robust and viable.

EXPERIMENTAL AND SIMULATION DETAILS

Fabrication and Measurement of Test Structures. As-sawn n-type Czochralski (n-Cz) Si(100) wafers with a 3.5 Ω·cm resistivity, ~180 μm in thickness, were laser scribed into 30 mm × 50 mm pieces

https://doi.org/10.1021/acsaem.1c01775
ACS Appl. Energy Mater. XXXX, XXX, XXX−XXX

Pursuant to the DOE Public Access Plan, this document represents the authors' peer-reviewed, accepted manuscript. The published version of the article is available from the relevant publisher.

and etched in 22.5% aqueous KOH to planarize the surface and remove the saw damage. The wafers were then cleaned with standard piranha, RCA 1 and RCA 2 steps, followed by etching in 1% HF to remove the oxide formed during the RCA 2. For IBC cells, a thin ∼1.5 nm SiO_x was then grown for ∼5 min in a quartz tube furnace at atmospheric pressure and 700 °C in ambient N_2/O_2 with a 3000:500 standard cm^3/min (sccm) flow rate ratio. For test structures, a ∼70 nm thick SiO_2 layer was grown instead for 30 min in the same furnace at atmospheric pressure and 1100 °C in ambient O_2 at a flow rate of 3000 sccm. After the growth of the oxide, a blanket intrinsic a-Si:H layer was deposited. To form n- and p-type-doped fingers, additional P- or B- heavily doped a-Si:H films were deposited onto the intrinsic a-Si:H through in-house fabricated c-Si shadow masks as described previously in ref 24. This method can achieve alignment precision ∼10 μm for the 30 × 50 mm^2 samples used in this study, but may be more difficult at the wafer scale. The a-Si:H was then crystallized at 850 °C, forming ∼10 nm grains.[37] This film was passivated with Al_2O_3 grown by atomic layer deposition from trimethyl aluminum and H_2O, which was subsequently annealed in forming gas at 400 °C[38] and then chemically removed from the backside. Electrical contacts to the patterned doped poly-Si fingers were formed by thermally evaporating ∼1 μm thick Al using via a Si shadow mask aligned with the doped poly-Si fingers. Following metallization of the cells, a ∼70 nm thick antireflection coating of SiN_x (refractive index ∼2) was grown via PECVD on the front of the devices from a 4:24 sccm SiH_4/NH_3 feed gas mixture at 400 mTorr, 200 °C substrate temperature, and a plasma power of 16 mW/cm^2. After metallization of the test structures by thermal evaporation, the coplanar resistance of the poly-Si film between the p- and n-type doped poly-Si fingers was determined using current−voltage measurements across the interdigitated fingers.

Scanning Probe Microscopy. The poly-Si isolation region between the p- and n-type fingers of the metallized IBC cells was characterized with SSRM[39] (Veeco Instruments Dimension 5000 scanning probe microscope with a Bruker SSRM Module) to determine local resistivity at several points between the n- and p-type fingers. The microscope was housed in an Ar glovebox (<0.1 ppm O_2, <0.1 ppm H_2O) to prevent oxidation of the samples. Probes with a conductive wear resistant diamond coating (Bruker DDESP-V2 nanoelectrical), ∼30 nm in radius, were used in the SSRM measurements at an applied direct current bias of −1 V. SSRM scans across a poly-Si isolation region were conducted incrementally in 20 × 5 μm scan areas at a fast scan axis angle of 90°. These scans were carried out along 32 lines with 128 sampling points per line at a scan rate of 0.1 Hz. A line scan of resistance across the region between doped fingers was obtained by averaging the 32 points at each lateral location. High-resolution 1 × 1 μm size scans (Figure 3d−f) were captured in three representative locations in the poly-Si region along 128 lines with 128 sampling points per line at scan rates of 0.3 and 0.6 Hz, respectively.

KPFM was employed for potential imaging[39] of the metallized test structures grown on ∼70 nm thick SiO_2. In our setup, the first resonant oscillation of the conductive atomic force microscopy (AFM) cantilever (50−70 kHz) was used for noncontact AFM (Veeco D5000 and Nanoscope V) topographic imaging. The second resonant frequency (300−500 kHz) was used for the potential imaging, which gives an enhanced energy resolution of ∼10 mV. A Pt-coated Si probe was used for the measurement with an applied reverse bias of 0.8 V between the probe and substrate.

Time of Flight Secondary Ion Mass Spectrometry. Three-dimensional (3-D) dopant concentration on top of the intrinsic a-Si:H layer was mapped prior to crystallization and metallization using time-of-flight secondary ion mass spectrometry (SIMS) (ION-TOF TOF-SIMS V). The primary ion beam was a 30 keV BiMn source, with a pulsed beam current of 1 pA. Measurements were performed in negative polarity utilizing a Cs^+ gun for sputtering, operating at 3 kV at a current of 25 nA. The data were quantified using relative sensitivity factors for phosphorous and boron in silicon obtained from separate measurements of an ion implanted standard.

Simulations. Carrier transport from n- to p-type poly-Si finger through a thin, wide isolation region formed by a partially contaminated thin intrinsic poly-Si film is a 3-D problem. Here, for simplicity, we conducted 1-D calculations assuming uniform dopant concentration throughout the thickness of the poly-Si film, and neglecting the finite thickness of the film that introduces additional boundary conditions and modifies space charge effects. We simulate the behavior of the p−i−n structure (see Figure 1b) through two models, a series resistor model and a p−i−n diode model. For a high shunt resistance, the p−i−n structure can most simply be modeled as a resistor, accounting for only carrier drift currents in the material. More accurately, this p−i−n structure has to be modeled as a planar diode, accounting for carrier drift, diffusion, space charge effects, and trapping into defects. Thus, we also performed finite element simulations for the diode behavior. Our device structure contained heavily doped n- and p-type poly-Si regions separated by a contaminated poly-Si (nominally intrinsic) isolation region with dopant profiles extending into it. A uniform density of trap defects, N_t, was introduced throughout the whole structure (doped and intrinsic regions). Within these diode simulations, such traps were introduced at six discrete energy levels (0.275, 0.33, and 0.385 eV from both band edges[40−42]) and electron and hole capture cross sections are kept constant for all trap states.[43]

Dopant profiles were input into the simulation based on the SIMS data or assumed to be an error function. For total dopant concentrations in poly-Si of 10^{20}−10^{21} cm^{-3}, ∼10% of boron atoms and ∼30% of phosphorus atoms are active.[38] To account for trap states in poly-Si,[44] we subtract the trap density, N_t, from the net dopant concentration to determine the effective dopant concentration, n_{eff} (see Figure 1b). The local resistivity in the p−i−n structure was obtained either from the literature[33,34,36] or estimated based on the carrier concentration and mobility in poly-Si. The resistivity was determined for different isolation region widths, δ, over the range of 20−55 μm[15,22,45] and for different characteristic diffusion lengths, L_{diff}, over the range 50−100 μm (see Supporting Information).

Using finite element simulations of a 1-D p−i−n structure, we simultaneously solved the Poisson's equation and the drift-diffusion equations for electrons and holes. In our model, the error function dopant profiles extend from the edges of the doped regions that were separated by 110 μm. This model also accounts for Shockley-Reed Hall (SRH) carrier recombination and emission. The characteristic decay lengths of 125 and 200 μm were used for boron and phosphorus tails, respectively. The recombination models and energy level definitions are shown in the Supporting Information. Additional parameters are also shown in the Supporting Information.

RESULTS AND DISCUSSION

Figure 1c shows the current−voltage curve of a planarized IBC cell with ∼10^{19} cm^{-3} dopant contamination across the intrinsic isolation region. Despite this level of contamination, the nearly flat slope of the curve at J_{sc} is indicative of a high shunt resistance. Suns−V_{oc} measurements show this resistance to be roughly 54 kΩ·cm^2, resulting in only a 0.03% loss in FF due to shunting, indicating that a strong compensation mechanism exists. To examine this more closely, the shunt resistance of the isolation region was directly measured for poly-Si IBC structures deposited on a thick insulating SiO_2 layer with isolation region widths of 10, 50, 100, and 200 μm (see Figure 2), with four samples for each region width. R_{shunt} increases approximately linearly with isolation region width. The error in R_{shunt} measurement between each of the four samples likely results from nonuniformities in dopant spreading along the length of the fingers. The measured R_{shunt} across the structure thus provides an estimate of the acceptable isolation region widths, which can be used for the masked PECVD dopant

https://doi.org/10.1021/acsaem.1c01775
ACS Appl. Energy Mater. XXXX, XXX, XXX−XXX

Pursuant to the DOE Public Access Plan, this document represents the authors' peer-reviewed, accepted manuscript.
The published version of the article is available from the relevant publisher.

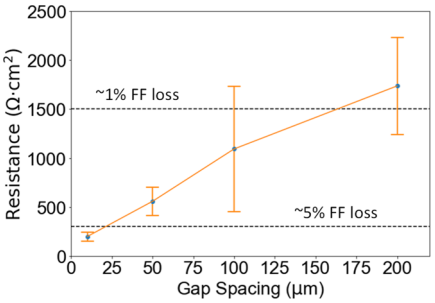

Figure 2. Shunt resistance of IBC test structures created with different intrinsic isolation region widths. The dotted lines correspond to R_{shunt} values, where FF would decrease by approximately 1 and 5% according to eq 1.

patterning technique: without any dopant mitigation,[24] R_{shunt} may become an issue at ~100 μm spacing.

Figure 3a shows a schematic of the SSRM setup used to measure the spreading resistance, R_s. The total resistance in the circuit $R_{tot} = R_c + R_s + R_b$, where R_c is the contact resistance between the probe and the sample, R_s is the spreading resistance within the sample, and R_b is the contact resistance at the back of the sample.

Experimental Observations of High R_{shunt} Due to a Wide Compensated Region. Figure 3b shows two overlapping lateral boron and phosphorus SIMS profiles in a 175 μm wide isolation region—the same isolation region width used in the cell of Figure 1c. Although the SIMS profiles were measured on as-deposited a-Si:H silicon before crystallization, the proportion of dopants, which diffuse into the bulk of the wafer after crystallization, is low compared to the amount, which remains in poly-Si (a few percent for phosphorus and less than 1% for boron),[38] so we expect these profiles to be representative of poly-Si as well. Because the probe used for SSRM is a few 10 s of nanometers wide, a high force is required on the probe tip to keep R_c low and the high contact area at the back of the device keeps R_b low. With low R_c and R_b, spreading resistance typically dominates the resistance measured. With these assumptions, resistivity ρ_{poly} at each point of the film can be approximated using $\rho_{poly} = R_{tot} \cdot 4 \cdot r_{eff}$, for a cylindrical contact geometry,[39,46] where R_{tot} is the local measured resistance and r_{eff} is the effective radius of the probe tip in contact with the substrate at this location. Importantly, the spreading resistance is dominated by the local ρ_{poly} of the film in the tip vicinity, which is proportional to its contact radius. Figure 3b shows a 175 μm isolating poly-Si line measured by SIMS, where the phosphorus dopant tail is at a much higher concentration than boron. Importantly, Figure 3c reveals the existence of a ~25 μm wide region of much higher resistivity than the rest of the contaminated isolation region. This is much wider than would be expected if direct dopant compensation was the only effect at play. The three 1 × 1 μm scans in Figure 3d–f show the resistivity in three locations within the isolating poly-Si line. In particular, the scan in Figure 3e was recorded at ~30 μm from the edge of the p-type-doped finger. The spreading resistance in this region is almost 3 orders of magnitude higher than the resistance measured closer to the edge of the p- or n-type finger. The local fluctuations in R_s in the scans in Figure 3d–f may be a combined effect of the surface roughness and grain boundaries in the poly-Si, which can change the degree of local compensation due to spatial variations in density of trap defects. This local variation in the trap state density likely influences the free carriers available for conduction, and therefore R_s.

Typical SSRM measurements are conducted on polished samples, so high probe forces (~10 s μN) can be used. However, our samples have a roughness on the order of several microns (see the optical image in Figure S1) due to mesas created during saw damage removal. Therefore, lower probe forces (1–2 μN) were used to prevent excessive wear on the diamond probe. A lower probe force results in a smaller effective tip radius, which increases the R_c between the

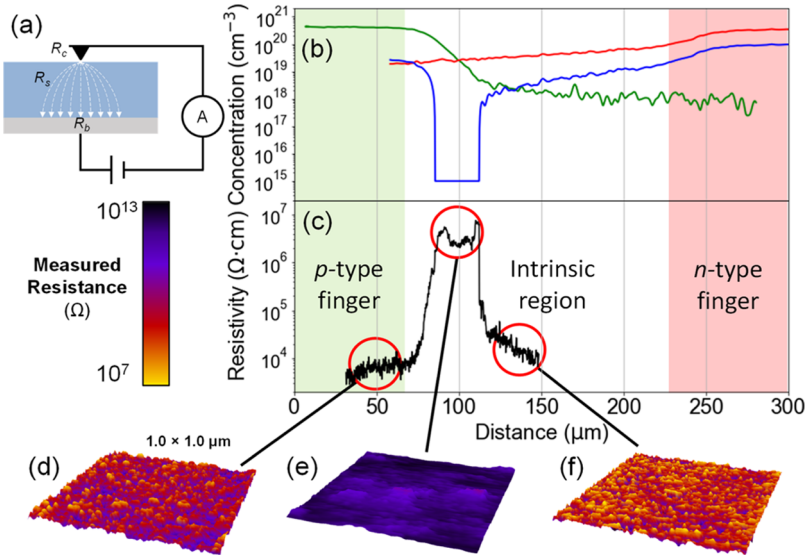

Figure 3. (a) Schematic of the SSRM setup. (b) TOF-SIMS measurements of overlapping p- (green) and n-type (red) PECVD a-Si:H tails with calculated n_{eff} (blue). All curves have been smoothed to reduce noise. (c) Resistivity as a function of distance between the p- and n-type fingers measured by SSRM. (d–f) SSRM heat maps showing measurements of resistance in three 1 μm^2 portions of the ~175 μm wide intrinsic poly-Si isolation region: a region dominated by boron (d), a compensated region where the dopant concentration is nearly equal (e), and a region dominated by phosphorus (f).

https://doi.org/10.1021/acsaem.1c01775
ACS Appl. Energy Mater. XXXX, XXX, XXX–XXX

Pursuant to the DOE Public Access Plan, this document represents the authors' peer-reviewed, accepted manuscript.
The published version of the article is available from the relevant publisher.

substrate and probe tip.[39] This is why the resistivity of the highly doped regions calculated from the SSRM data in Figure 3c is unrealistically high. However, relative changes in the spreading resistance measured by SSRM are more accurate than absolute resistance values.

The local work function across the isolation region was measured using KPFM (see Figure 4). On the p- and n-type

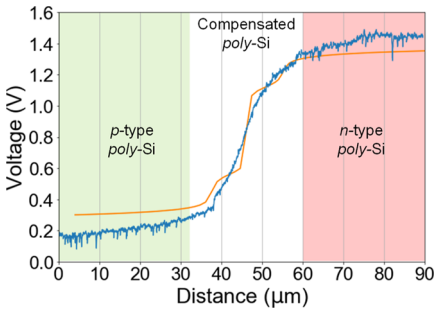

Figure 4. KPFM scan across the poly-Si isolation region of an IBC test structure (blue) compared to a simulated potential profile of overlapping error function profiles (orange). The left side shaded in green corresponds to the region of the intrinsic gap contaminated primarily by boron (green), while the right side shaded in red corresponds to the region of the intrinsic gap contaminated primarily by phosphorus (red).

sides of the poly-Si isolation region, the work functions remain relatively flat, with a gradual potential change occurring over the range of ~35−60 μm, where the dopant concentrations are expected to be nearly equal. This is indicative of a depletion region in the p−i−n structure. The width and location of the depletion region is ~25 μm, which agrees well with the width of the high resistivity region measured by SSRM. However, given the high doping concentrations at the point of overlap (see Figure 3b), the depletion width should be on the order of a few nanometers. To understand why SSRM shows a wide high resistivity region and why KPFM shows a gradual increase in potential, we account for the existence of trap states in poly-Si, which are most likely present in the grain boundaries. These trap states[34,40,47,48] capture charge carriers, which creates a potential barrier for transport through the conduction or valence bands, causing a reduction of carrier mobility.[44,47] The reduction in carrier mobility is the highest when the Fermi energy of poly-Si is close to the energy levels of the trap state[35,40] and the net carrier concentration is approximately equal to N_t. In addition to the reduction in mobility from potential barriers at grain boundaries, mobility is further lowered due to scattering of carriers off the ionized dopants within the poly-Si.[49] We speculate that this effect could be further enhanced by the existence of both phosphorus and boron ions within the compensated region.[49,50] In summary, dopant compensation, combined with the high N_t in poly-Si enable the formation of a high resistivity region that is several 10 s of μm in width.

Simple Resistor Model with Trap-Assisted Compensation. As a simplest case for incorporating traps into the resistor model, we calculate n_{eff} by subtracting the trap density from the local net active doping concentration. From this, we can calculate the local resistivity as described in the Experimental and Simulation Details section. This simple model does not account for carrier diffusion, potential gradients, or SRH carrier recombination and emission. Figure 5 shows the local resistivity as a function of position in the poly-Si isolation region calculated for two values of trap

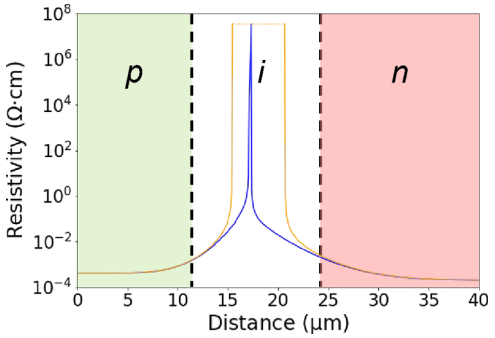

Figure 5. Resistivity as a function of location in the isolation region depicted in Figure 1b for two values of $N_t = 10^{17}$ cm^{-3} (blue) and 10^{19} cm^{-3} (orange). The flat, dotted portion of the orange curve represents resistivity values significantly higher than those shown but is cut off for simplicity.

density—10^{17} and 10^{19} cm^{-3}—using the n- and p-type dopant profiles described by error functions (see Figure 1b), and the series resistance model described above. These curves show that the majority of the isolation region can have low local resistivity because of the high net doping concentration for either boron or phosphorus. However, the region over which the dopant profiles overlap in concentration creates a compensated region with a local resistivity that is several orders of magnitude higher than the surrounding regions. Increasing trap density widens this compensated region significantly, see Figure 5b. Calculating R_{shunt} from the series resistance model yields values of ~9×10^9 and ~7×10^{12} Ω·cm^2 for assumed N_t of 10^{17} and 10^{19} cm^{-3}, respectively. The simplified model shows that this narrow region of high resistivity results in a high shunt resistance between the doped p- and n-type fingers. Although the calculated resistances from this model are quite high, for $N_t = 10^{17}$ cm^{-3}, the region is very narrow, ~1 μm, and is likely not sufficient to prevent shunting along the entire length of the doped fingers due to nonuniformities along the finger and defect states within poly-Si possibly allowing conduction via hopping between nearby defect states.[51] However, for $N_t = 10^{19}$ cm^{-3}, the compensated region is much wider and will likely prevent shunting between the fingers.

Using the simple resistor model, we also simulated the resistivity for the poly-Si isolation region for the experimentally measured dopant profiles (see Figure 3b). Comparing the simulated n_{eff} in Figure 3b with the local resistivity measured with SSRM in Figure 3c, we see that the localization of the highly resistive region coincides well with the region of low n_{eff}. Thus, this simple resistor model captures the main experimental feature—the presence of a very wide compensated region. Using this simulation methodology, we calculated a shunt resistance of ~10^9 Ω·cm^2 for our experimentally measured dopant profiles. For the dopant tails reported in ref 20, we calculate $R_{shunt} \approx 8$ MΩ·cm^2 across a 30 μm wide isolation region, which is on the same order of magnitude as reported by these authors in ref 15. While the resistor model is clearly an imperfect approximation, it appears to be suitable to estimate the location, width, and approximate R_{shunt} of the compensated region. We have further shown that this simple approximation can be used to determine the required width of

https://doi.org/10.1021/acsaem.1c01775
ACS Appl. Energy Mater. XXXX, XXX, XXX−XXX

Pursuant to the DOE Public Access Plan, this document represents the authors' peer-reviewed, accepted manuscript.
The published version of the article is available from the relevant publisher.

the intrinsic poly-Si isolation region based on different values of the effective diffusion lengths for n- and p-type dopants (see Figures S2 and S3).

Refined Drift, Diffusion, and Recombination Model for Trap-Assisted Compensation. Although the resistor model seems to predict well the location and width of the compensated portion of the isolation region between p- and n-type fingers, the direct contact of the doped tails[49] is more akin to a p−i−n diode. Our more advanced model and simulations included a full set of semiconductor equations including carrier drift, diffusion, recombination, and space charge effects. In these simulations, we determined the effect of N_t on n_{eff}, and generated $I-V$ curves as described in the Experimental and Simulation Details section. The material properties and parameters used in the simulation are included in the Supporting Information. For a net dopant concentration of $\sim 10^{19}$ cm^{-3}, but with no trap states, the potential abruptly changes over a distance of only a few nanometers, which is inconsistent with the KPFM measurements in Figure 4. However, introducing trap states within the bandgap, we obtained close to excellent agreement with the KPFM results. The potential profile generated within the diode simulations is shown in Figure 4. In this model, we introduced six trap levels within the bandgap[43] (see the Experimental and Simulation Details section). We obtained better agreement with experiments using six trap states compared to the case where only one trap state was considered. The simulation results still do not perfectly match the measured potential profile and could be improved by introducing a continuous distribution of trap states, more accurate capture cross sections, and 2- or 3-D simulations of a thin film structure on a flat substrate.

Figure 6a shows the simulated band diagram of the p−i−n structure with the six trap states. These discrete trap states instead of a continuum of states cause the abrupt steps in the valence and conduction band edges in the isolation region. For a set of n- and p-type dopant concentration profiles in the isolation region, Figure 6b shows n_{eff} (dashed lines) for three values of N_t—2.3 × 10^{17}, 9 × 10^{17}, and 2.3 × 10^{18} cm^{-3}. Although N_t can vary significantly depending on the grain size of the poly-Si, these numbers are on the order reported in the literature.[33−36,40,47] As expected, n_{eff} drops more steeply as the net doping concentration approaches N_t. In agreement with the resistor model described previously, n_{eff} is roughly equal to the difference between net doping and N_t. This sharp drop occurs as almost all free carriers are trapped by defect states. As also predicted by the resistor model, the width of the compensated region widens with increasing N_t, resulting in a corresponding decrease in conductivity of the isolation region. This decrease in conductivity is apparent in Figure 7, which shows the $I-V$ curves for the p−i−n structure shown in Figure 6a for five different values of N_t. From the current−voltage curves with the assumed 1 mm^2 simulated cross-sectional area, total I_{shunt} was obtained by assuming a poly-Si film thickness of ~50 nm in 40, 2-cm-long, poly-Si isolation lines. For lower values of N_t, the $I-V$ curve resembles a more ideal p−i−n diode. With increasing N_t, more free carriers are captured in the trap states, which reduces the diode current by more than 2 orders of magnitude for a 1 order of magnitude increase in N_t at an operating current of 0.6 V (see Figure 7). Because the structure in Figure 6a can be approximated as an ideal diode in series with a resistor, the voltage drop across the p- and n-fingers is split between the diode and the resistor. As the applied voltage increases, the resistance of the diode drops

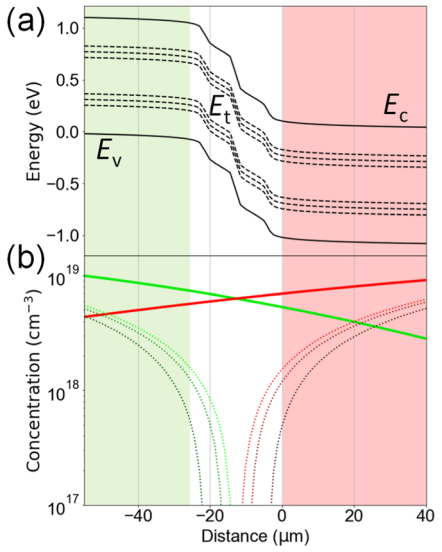

Figure 6. Simulated band diagram and effective carrier concentration profiles from the diode simulations. (a) Band diagram of the p−i−n structure under equilibrium for N_t = 2.3 × 10^{18} cm^{-3}. The dashed lines represent the energy levels of the six electron and hole traps within the bandgap used in these simulations. (b) Doping profiles of boron (solid green) and phosphorus (solid red) overlap in poly-Si with trap defect concentrations of 2.3 × 10^{17} cm^{-3}, 9 × 10^{17} cm^{-3}, and 2.3 × 10^{18} cm^{-3}. Dotted curves represent the free electron (red) and hole (green) concentrations for each level of trap density, with the lightest colors corresponding to the lowest trap density and the darkest colors corresponding to the highest trap density.

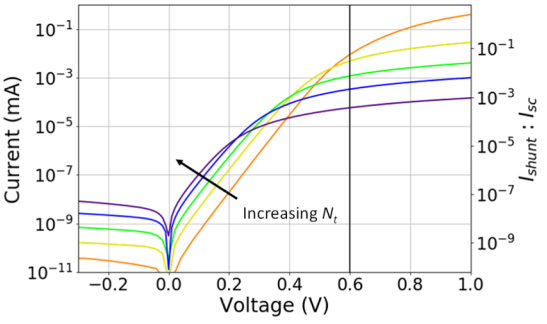

Figure 7. Current−voltage plots of simulated p−i−n diodes for various levels of trap defect density, N_t = 2.3 × 10^{17} (orange), 3 × 10^{17} (yellow), 4.95 × 10^{17} (green), 9 × 10^{17} (blue), and 2.3 × 10^{18} cm^{-3} (purple).

rapidly when the diode "turns on" and the resistor starts to dominate. The more defective diodes have a wider compensated region, and thus a stronger resistive behavior, resulting in an earlier transition from the diode behavior to resistor behavior than for less-defective isolation regions. The isolation region with the highest N_t (2.3 × 10^{18} cm^{-3}) still shows the diode behavior, but only at low forward bias voltages up to 0.2 V. Above that, it approximately resembles a resistor. Moreover, the leakage current through this highly defective region at 0.6 V, which is close to the voltage at the maximum power point of a c-Si solar cell, is 2 orders of magnitude lower than for the lowest value of N_t (2.3 × 10^{17} cm^{-3}), and the shunting current (see right axis of Figure 7) is just 10^{-4} × I_{sc} of the cell (assumed as 40 mA/cm^2). Therefore, we expect that even dopant contamination levels as high as ~10^{19} cm^{-3} can be tolerated during processing, and result in no significant loss in

https://doi.org/10.1021/acsaem.1c01775
ACS Appl. Energy Mater. XXXX, XXX, XXX−XXX

Pursuant to the DOE Public Access Plan, this document represents the authors' peer-reviewed, accepted manuscript. The published version of the article is available from the relevant publisher.

FF as long as the N_t ($\sim 10^{18}$ cm^{-3}) is greater than the $N_{eff} = |N_a - N_d|$ across a width of ≥ 20 μm in the isolation region. For less-defective poly-Si films of a larger grain size used in poly-Si/SiO_x passivated contacts, such high levels of dopant contamination could lead to much higher losses in FF. In industrially fabricated cells, the poly-Si would likely be grown by low-pressure PECVD, with larger grain sizes, and hence fewer traps. Because of this, the dopant tails would need to have a much steeper drop in concentration or be steepened by some strategy such as a short etching step.[24] Depending on deposition and annealing conditions, however, poly-Si can have grain sizes ranging over several orders of magnitude,[52−54] and this processing parameter can be optimized to minimize the loss in FF due to dopant spreading in poly-Si/SiO_x passivating IBCs. Although moving to 2- or 3-D simulations would be necessary to accurately simulate complete devices, this 1-D model clearly demonstrates the primary effect which traps in poly-Si have in assisting dopant compensation.

Although these simulations were focused on a defective p−i−n junction between doped IBC fingers, they have implications for other poly-Si p−n junctions as well. For instance, as perovskite/c-Si tandem solar cells have gained interest, there has been work demonstrating the use of heavily-doped p^+−n^+ tunnel junctions as electrical connections between the top and bottom cells of the monolithic tandem devices.[55] Following high-temperature annealing of these junctions, interdiffusion between the doped films causes a degree of compensation in the tunnel junction. This could increase the series resistance across the junction depending on the degree of trap-assisted compensation. However, after rapid thermal processing of such junctions, very low junction resistivities are observed, which suggests that this dopant compensation becomes inactive due to annealing.[56] We attribute this difference in behavior compared to a p−i−n diode to the direct contact of the p^+ and n^+ regions with no intrinsic region between them. The lack of an intrinsic poly-Si region means that there is no physical space allowing for the doping concentrations to decay and reach a level as low as the defect density for trap-assisted compensation to take effect. Additionally, the interdiffusion of dopants across the tunnel junction can be suppressed with the addition of C and/or O to the interface.[57] Thus, this effect can be utilized when desired or avoided when not by specifying the distance between doped regions, the defect density, or the processing parameters, which lead to dopant overlap.

In complete IBC solar cells with poly-Si/SiO_x passivated contacts, there may also exist a diffused sheet of dopants within the c-Si base with $\sim 10^{19}$ cm^{-3} active dopant concentration but with nearly no defects to trap the charge carriers.[38] Therefore, direct contact of the opposite dopants within the c-Si base will form a true diode in the bulk Si. Assuming the overlap in dopants occurs at the same concentration as in the poly-Si with $\sim 10^{19}$ cm^{-3} dopants, the space charge region will be ~10 nm, which is still far too wide to allow for tunneling from the conduction band of the n-type side to the valence band of the p-type side. Because of this, we suspect that the diffused p−n diode will simply separate carriers toward their respective contacts, allowing for very little shunt current.

CONCLUSIONS

We examine the effect of contamination of the intrinsic isolation region between n- and p-type fingers in poly-Si/SiO_x IBC Si solar cells with dopant atoms to a level of $\sim 10^{19}$ cm^{-3} and show that despite this strong contamination, shunting does not occur in the devices and poly-Si test structures with similar IBC fingers. Our SSRM nanoprobe measurement confirms the existence of a ~25 μm high-resistivity compensated region within the nominally intrinsic poly-Si isolation region. This SSRM result is complemented by the KPFM data, which show a space charge region of the same width within the isolation region. A novel mechanism is proposed to explain how, despite significant dopant spreading in the entire isolation region between doped p- and n-type poly-Si fingers of IBC cells, low shunting is observed. These experimental results are explained by a trap-assisted compensation mechanism and confirmed by simulations. The first simulation model considers the isolation region very simply as a resistor with local resistivity governed by the difference between the trap density and the local net active doping concentration. This model accurately predicts the location and width of the compensated region to match the SSRM resistivity data. A much more accurate model treating the isolation region as a defective p−i−n diode is also considered by solving the Poisson's equation, the drift-diffusion equations for electrons and holes, capture and emission of carriers by traps, and SRH and auger recombination. Using this model, we similarly show that increasing the trap density by 1 order of magnitude from $\sim 10^{17}$ to $\sim 10^{18}$ cm^{-3} results in a decreased shunt current across the isolation region by 2 orders of magnitude to a level that does not affect cell performance. Demonstration of the formation of this resistive compensated region shows that the contamination of the intrinsic isolation region of IBC cells may not be as harmful as previously assumed, if the criteria described in these studies are met. Our results imply that the IBC cell based on poly-Si contacts has great industrial potential with a robust processing window.

ASSOCIATED CONTENT

Supporting Information

The Supporting Information is available free of charge at https://pubs.acs.org/doi/10.1021/acsaem.1c01775.

Surface morphology of the sample measured in SSRM; additional results obtained from our resistor simulation model; and more specific details regarding the resistor model and the diode simulations including specifically parameter values used and equations solved (PDF)

AUTHOR INFORMATION

Corresponding Authors

Sumit Agarwal − *Colorado School of Mines, Golden, Colorado 80401, United States; National Renewable Energy Laboratory, Golden, Colorado 80401, United States;* orcid.org/0000-0002-4453-3656; Email: sagarwal@mines.edu

Paul Stradins − *Colorado School of Mines, Golden, Colorado 80401, United States; National Renewable Energy Laboratory, Golden, Colorado 80401, United States;* Email: pauls.stradins@nrel.gov

Authors

Matthew B. Hartenstein − *Colorado School of Mines, Golden, Colorado 80401, United States; National Renewable Energy Laboratory, Golden, Colorado 80401, United States;* orcid.org/0000-0002-2207-2262

Pursuant to the DOE Public Access Plan, this document represents the authors' peer-reviewed, accepted manuscript. The published version of the article is available from the relevant publisher.

Caleb Stetson − *Colorado School of Mines, Golden, Colorado 80401, United States; National Renewable Energy Laboratory, Golden, Colorado 80401, United States;* orcid.org/0000-0003-0729-1261
William Nemeth − *National Renewable Energy Laboratory, Golden, Colorado 80401, United States*
Vincenzo LaSalvia − *National Renewable Energy Laboratory, Golden, Colorado 80401, United States*
Steven P. Harvey − *National Renewable Energy Laboratory, Golden, Colorado 80401, United States;* orcid.org/0000-0001-6120-7062
San Theingi − *National Renewable Energy Laboratory, Golden, Colorado 80401, United States*
Matthew Page − *National Renewable Energy Laboratory, Golden, Colorado 80401, United States*
Chun-Sheng Jiang − *National Renewable Energy Laboratory, Golden, Colorado 80401, United States;* orcid.org/0000-0003-0230-7500
Mowafak M. Al-Jassim − *National Renewable Energy Laboratory, Golden, Colorado 80401, United States*
David L. Young − *National Renewable Energy Laboratory, Golden, Colorado 80401, United States*

Complete contact information is available at: https://pubs.acs.org/10.1021/acsaem.1c01775

Notes

The authors declare no competing financial interest.

■ ACKNOWLEDGMENTS

This research was supported by US DOE EERE under the Photovoltaic Research and Development (PVRD) program of the Solar Energy Technology Office under Award Number DE-EE0007553 to the Colorado School of Mines. This work was authored in part by the National Renewable Energy Laboratory, operated by Alliance for Sustainable Energy, LLC, for the U.S. Department of Energy (DOE) under contract no. DE-AC36-08GO28308. Funding was provided by the U.S. Department of Energy Office of Energy Efficiency and Renewable Energy Solar Energy Technologies Office. The views expressed in the article do not necessarily represent the views of the DOE or the U.S. Government. The U.S. Government retains and the publisher, by accepting the article for publication, acknowledges that the U.S. Government retains a nonexclusive, paid-up, irrevocable, and worldwide license to publish or reproduce the published form of this work, or allow others to do so, for U.S. Government purposes.

■ REFERENCES

(1) Metz, A.; Fischer, M.; Trube, J. International technology roadmap for photovoltaics (ITRPV): Crystalline silicon technology-current status and outlook. *Proceedings of the PV Manufacturing in Europe Conference, Brussels, Belgium*, 2017; pp 18−19.
(2) Haase, F.; Hollemann, C.; Schäfer, S.; Merkle, A.; Rienäcker, M.; Krugener, J.; Brendel, R.; Peibst, R. Laser contact openings for local poly-Si-metal contacts enabling 26.1%-efficient POLO-IBC solar cells. *Sol. Energy Mater. Sol. Cells* **2018**, *186*, 184−193.
(3) Lindholm, F. A.; Neugroschel, A.; Arienzo, M.; Iles, P. A. Heavily doped polysilicon-contact solar cells. *IEEE Electron. Device Lett.* **1985**, *6*, 363−365.
(4) Yoshikawa, K.; Yoshida, W.; Irie, T.; Kawasaki, H.; Konishi, K.; Ishibashi, H.; Asatani, T.; Adachi, D.; Kanematsu, M.; Uzo, H.; Yamamoto, H. Exceeding conversion efficiency of 26% by heterojunction interdigitated back contact solar cell with thin film Si technology. *Sol. Energy Mater. Sol. Cells* **2017**, *173*, 37−42.
(5) Yoshikawa, K.; Kawasaki, H.; Yoshida, W.; Irie, T.; Konishi, K.; Nakano, K.; Uto, T.; Adachi, D.; Kanematsu, M.; Uzo, H.; Yamamoto, H. Silicon heterojunction solar cell with interdigitated back contacts for a photoconversion efficiency over 26%. *Nat. Energy* **2017**, *2*, 17032.
(6) Aberle, A. G.; Glunz, S. W.; Stephens, A. W.; Green, M. A. High-efficiency silicon solar cells: Si/SiO2, interface parameters and their impact on device performance. *Prog. Photovoltaics Res. Appl.* **1994**, *2*, 265−273.
(7) Aberle, A. G. Surface passivation of crystalline silicon solar cells: a review. *Prog. Photovoltaics Res. Appl.* **2000**, *8*, 473−487.
(8) Rienäcker, M.; Bossmeyer, M.; Merkle, A.; Römer, U.; Haase, F.; Krugener, J.; Brendel, R.; Peibst, R. Junction resistivity of carrier-selective polysilicon on oxide junctions and its impact on solar cell performance. *IEEE J. Photovolt.* **2016**, *7*, 11−18.
(9) Peibst, R.; Römer, U.; Larionova, Y.; Rienäcker, M.; Merkle, A.; Folchert, N.; Reiter, S.; Turcu, M.; Min, B.; Krugener, J.; Tetzlaff, D.; Bugiel, E.; Wietler, T.; Brendel, R. Working principle of carrier selective poly-Si/c-Si junctions: Is tunnelling the whole story? *Sol. Energy Mater. Sol. Cells* **2016**, *158*, 60−67.
(10) van der Vossen, R.; Feldmann, F.; Moldovan, A.; Hermle, M. Comparative study of differently grown tunnel oxides for p-type passivating contacts. *Energy Procedia* **2017**, *124*, 448−454.
(11) Kale, A. S.; Nemeth, W.; Guthrey, H.; Kennedy, E.; Norman, A. G.; Page, M.; Al-Jassim, M.; Young, D. L.; Agarwal, S.; Stradins, P. Understanding the charge transport mechanisms through ultrathin SiOx layers in passivated contacts for high-efficiency silicon solar cells. *Appl. Phys. Lett.* **2019**, *114*, 083902.
(12) Feldmann, F.; Simon, M.; Bivour, M.; Reichel, C.; Hermle, M.; Glunz, S. W., Carrier-selective contacts for Si solar cells, *Appl. Phys. Lett.*, vol. *104*, no. 18, **2014**, doi: DOI: 10.1063/1.4875904.
(13) Haase, F.; Kiefer, F.; Schäfer, S.; Kruse, C.; Krugener, J.; Brendel, R.; Peibst, R. Interdigitated back contact solar cells with polycrystalline silicon on oxide passivating contacts for both polarities. *Jpn. J. Appl. Phys.* **2017**, *56*, 08MB15.
(14) Haase, F.; Schafer, S.; Klamt, C.; Kiefer, F.; Krugener, J.; Brendel, R.; Peibst, R. Perimeter Recombination in 25%-Efficient IBC Solar Cells With Passivating POLO Contacts for Both Polarities. *IEEE J. Photovolt.* **2018**, *8*, 23−29.
(15) Hollemann, C.; Haase, F.; Schäfer, S.; Krugener, J.; Brendel, R.; Peibst, R. 26.1%-efficient POLO-IBC cells: Quantification of electrical and optical loss mechanisms. *Prog. Photovoltaics Res. Appl.* **2019**, *27*, 950.
(16) Rienäcker, M.; Merkle, A.; Römer, U.; Kohlenberg, H.; Krugener, J.; Brendel, R.; Peibst, R. Recombination Behavior of Photolithography-free Back Junction Back Contact Solar Cells with Carrier-selective Polysilicon on Oxide Junctions for Both Polarities. *Energy Procedia* **2016**, *92*, 412−418.
(17) Hollemann, C.; Haase, F.; Rienäcker, M.; Barnscheidt, V.; Krugener, J.; Folchert, N.; Brendel, R.; Richter, S.; Großer, S.; Sauter, E.; Hubner, J.; Oestreich, M.; Peibst, R. Separating the two polarities of the POLO contacts of an 26.1%-efficient IBC solar cell. *Sci. Rep.* **2020**, *10*, 658.
(18) Liu, J.; Yao, Y.; Xiao, S.; Gu, X. Review of status developments of high-efficiency crystalline silicon solar cells. *J. Phys. D: Appl. Phys.* **2018**, *51* (12), 123001.
(19) Tachibana, T.; Tanahashi, K.; Mochizuki, T.; Shirasawa, K.; Takato, H. Bifacial interdigitated-back-contact (IBC) crystalline silicon solar cell: fabrication and evaluation by internal quantum efficiency mapping. *2018 IEEE 7th World Conference on Photovoltaic Energy Conversion (WCPEC) (A Joint Conference of 45th IEEE PVSC, 28th PVSEC & 34th EU PVSEC)*, 2018; pp 3738−3742.
(20) Tomihisa, T.; Shirasawa, K.; Takato, H. Investigation of electrical shading loss of bifacial interdigitated-back-contact (IBC) crystalline silicon solar cells with screen-printed electrode. *Jpn. J. Appl. Phys.* **2020**, *59*, 116503.
(21) Kopecek, R.; Libal, J.; Lossen, J.; Mihailetchi, V. D.; Chu, H.; Peter, C.; Buchholz, F.; Wefringhaus, E.; Halm, A.; Ma, J.; Jianda, L.; Yonggang, G.; Xiaoyong, Q.; Xiang, W.; Peng, D. ZEBRA technology:

Pursuant to the DOE Public Access Plan, this document represents the authors' peer-reviewed, accepted manuscript. The published version of the article is available from the relevant publisher.

low cost bifacial IBC solar cells in mass production with efficiency exceeding 23.5%. *2020 47th IEEE Photovoltaic Specialists Conference (PVSC), 15 June-21 Aug. 2020*, 2020; pp 1008−1012.
(22) Reichel, C.; Muller, R.; Feldmann, F.; Richter, A.; Hermle, M.; Glunz, S. W. Influence of the transition region between p- and n-type polycrystalline silicon passivating contacts on the performance of interdigitated back contact silicon solar cells. *J. Appl. Phys.* **2017**, *122*, 184502.
(23) Green, M. A. Solar cells: operating principles, technology, and system applications/Martin A. *Green Prentice-Hall Series in Solid State Physical Electronics*; Prentice-Hall: Englewood Cliffs, N.J, 1982 no accessed from https://nla.gov.au/nla.cat-vn1555330.
(24) Hartenstein, M. B.; Nemeth, W.; LaSalvia, V.; Harvey, S.; Guthrey, H.; Theingi, S.; Page, M.; Young, D. L.; Stradins, P.; Agarwal, S. Isolating p- and n- Doped Fingers with Intrinsic poly-Si in Passivated Interdigitated Back Contact Silicon Solar Cells. *IEEE J. Photovolt.* **2020**, *10*, 1574.
(25) Fell, A.; Fong, K. C.; McIntosh, K. R.; Franklin, E.; Blakers, A. W. 3-D Simulation of Interdigitated-Back-Contact Silicon Solar Cells With Quokka Including Perimeter Losses. *IEEE J. Photovolt.* **2014**, *4*, 1040−1045.
(26) Fell, A.; McIntosh, K. R.; Altermatt, P. P.; Janssen, G. J. M.; Stangl, R.; Ho-Baillie, A.; Steinkemper, H.; Greulich, J.; Muller, M.; Min, B.; Fong, K. C.; Hermle, M.; Romijn, I. G.; Abbott, M. D. Input Parameters for the Simulation of Silicon Solar Cells in 2014. *IEEE J. Photovolt.* **2015**, *5*, 1250−1263.
(27) Procel, P.; Yang, G.; Isabella, O.; Zeman, M. Numerical Simulations of IBC Solar Cells Based on Poly-Si Carrier-Selective Passivating Contacts. *IEEE J. Photovolt.* **2019**, *9*, 374−384.
(28) Lu, M.; Das, U.; Bowden, S.; Hegedus, S.; Birkmire, R. Optimization of interdigitated back contact silicon heterojunction solar cells: tailoring hetero-interface band structures while maintaining surface passivation. *Prog. Photovoltaics Res. Appl.* **2011**, *19*, 326−338.
(29) Budhraja, V.; Devayajanam, S.; Basnyat, P. Simulation Results: Optimization of Contact Ratio for Interdigitated Back-Contact Solar Cells. *Int. J. Photoenergy* **2017**, *2017*, 1−10.
(30) Mizutani, H.; Koizumi, T. Diode and Semiconductor Device Having a Controlled Intrinsic or Low Impurity Concentration Region between Opposite Conductivity Type Semiconductor Regions, Google Patents, US5616944A, 1997.
(31) Eguchi, T.; Matsumoto, T.; Fujita, S. Thin Film Semiconductor Device and Method of Manufacturing the Same, Electro-Optical Device, and Electronic Apparatus, Google Patents, US20060017139A1, 2006.
(32) Lu, J.; Apte, R. B. Gated Co-planar Poly-Silicon Thin Film Diode, Google Patents, US8384180B2, 2013.
(33) Tyagi, B. P.; Sen, K. On the resistivity of polycrystalline silicon. *Phys. Status Solidi A* **1983**, *80*, 679−684.
(34) Joshi, D. P.; Srivastava, R. S. Mobility and carrier concentration in polycrystalline silicon. *Sol. Cell.* **1984**, *12*, 337−344.
(35) Lombos, B. A. Deep levels in semiconductors. *Can. J. Chem.* **1985**, *63*, 1666−1671.
(36) Fripp, A. L. Dependence of resistivity on the doping level of polycrystalline silicon. *J. Appl. Phys.* **1975**, *46*, 1240−1244.
(37) Young, D. L.; Nemeth, W.; LaSalvia, V.; Page, M. R.; Theingi, S.; Aguiar, J.; Lee, B. G.; Stradins, P. Low-cost plasma immersion ion implantation doping for Interdigitated back passivated contact (IBPC) solar cells. *Sol. Energy Mater. Sol. Cells* **2016**, *158*, 68−76.
(38) Nemeth, B.; Young, D. L.; Page, M. R.; Lasalvia, V.; Johnston, S.; Reedy, R.; Stradins, P. Polycrystalline silicon passivated tunneling contacts for high efficiency silicon solar cells. *J. Mater. Res.* **2016**, *31*, 671−681.
(39) Kalinin, S. V.; Gruverman, A. *Scanning Probe Microscopy: Electrical and Electromechanical Phenomena at the Nanoscale*; Springer Science & Business Media, 2007.
(40) Lombos, B.; Yee, S.; Pietrantonio, M.; Averous, M. Grain boundaries introduced deep levels in polysilicon. *J. Phys. Colloq.* **1982**, *43*, C1199−C1206.
(41) Ayres, J. R. Characterization of trapping states in polycrystalline-silicon thin film transistors by deep level transient spectroscopy. *J. Appl. Phys.* **1993**, *74*, 1787−1792.
(42) Criado, A.; Alonso, B.; Piqueras, J. Deep traps in polysilicon solar cells. *Electron. Lett.* **1978**, *14*, 622−623.
(43) Simmons, J. G.; Taylor, G. W. Nonequilibrium Steady-State Statistics and Associated Effects for Insulators and Semiconductors Containing an Arbitrary Distribution of Traps. *Phys. Rev. B: Condens. Matter Mater. Phys.* **1971**, *4*, 502−511.
(44) Kamins, T. I. Hall mobility in chemically deposited polycrystalline silicon. *J. Appl. Phys.* **1971**, *42*, 4357−4365.
(45) Young, D. L.; Nemeth, W.; LaSalvia, V.; Reedy, R.; Essig, S.; Bateman, N.; Stradins, P. Interdigitated Back Passivated Contact (IBPC) Solar Cells Formed by Ion Implantation. *IEEE J. Photovolt.* **2016**, *6*, 41−47.
(46) Dickens, L. E. Spreading Resistance as a Function of Frequency. *IEEE Trans. Microw. Theor. Tech.* **1967**, *15*, 101−109.
(47) Seto, J. Y. W. The electrical properties of polycrystalline silicon films. *J. Appl. Phys.* **1975**, *46*, 5247−5254.
(48) Lu, N. C.-C.; Gerzberg, L.; Chih-Yuan Lu, C.-Y.; Meindl, J. D. Modeling and optimization of monolithic polycrystalline silicon resistors. *IEEE Trans. Electron. Dev.* **1981**, *28*, 818−830.
(49) Neamen, D. *Semiconductor Physics and Devices: Basic Principles*, 4th ed.; McGraw-Hill Higher Education, 2011.
(50) Kar, R. K.; Mukherjee, M. N. Electron mobility in compensated semiconductors at low temperatures. *Z. Phys.* **1970**, *237*, 16−20.
(51) Schmidlin, F. W. Kinetic theory of hopping transport. *Phil. Mag. B* **1980**, *41*, 535−570.
(52) Stoffel, A.; Kovács, A.; Kronast, W.; Muller, B. LPCVD against PECVD for micromechanical applications. *J. Micromech. Microeng.* **1996**, *6*, 1−13.
(53) Hatalis, M. K.; Greve, D. W. Large grain polycrystalline silicon by low-temperature annealing of low-pressure chemical vapor deposited amorphous silicon films. *J. Appl. Phys.* **1988**, *63*, 2260−2266.
(54) French, P. J.; Evans, A. G. R. Effect of deposition temperature on LPCVD polysilicon. *Electron. Lett.* **1986**, *22*, 716−718.
(55) Yan, L. L.; Han, C.; Shi, B.; Zhao, Y.; Zhang, X. D. A review on the crystalline silicon bottom cell for monolithic perovskite/silicon tandem solar cells. *Mater. Today Nano* **2019**, *7*, 100045.
(56) Luderer, C.; Reichel, C.; Feldmann, F.; Bivour, M.; Hermle, M. Passivating and low-resistive poly-Si tunneling junction enabling high-efficiency monolithic perovskite/silicon tandem solar cells. *Appl. Phys. Lett.* **2019**, *115*, 182105.
(57) Haug, F.-J.; Morisset, A.; Wyss, P.; Lehmann, M.; Hessler-Wyser, A.; Jeangros, Q.; Ingenito, A.; Ballif, C.; Kumar, C. N. S.; Eswara, S.; Valle, N. Passivating Polysilicon Recombination Junctions for Crystalline Silicon Solar Cells. *Phys. Status Solidi Rapid Res. Lett.* **2021**, 2100272.

https://doi.org/10.1021/acsaem.1c01775
ACS Appl. Energy Mater. XXXX, XXX, XXX−XXX